Science Advances
AAAS

Supplementary Materials for

Ultrahigh dielectric permittivity in oxide ceramics by hydrogenation

Nguyen X. Duong *et al.*

Corresponding author: Tae H. Kim, thkim79@ulsan.ac.kr

Sci. Adv. **9**, eadd8328 (2023)
DOI: 10.1126/sciadv.add8328

This PDF file includes:

Supplementary Text

X-ray absorption (XAS) measurements

To investigate the electronic properties of pure and Ni-substituted $BaTiO_3$ ceramics, we performed the X-ray absorption (XAS) measurements. In O *K*-edge spectra of pure $BaTiO_3$ ceramics, peaks A and B were respectively attributed to the transition from O 1*s* to t_{2g} and e_g hybridized states between O 2*p*-Ti 3*d*, which were separated by octahedral ligand field splitting (Fig. S1). The features C and D were due to O 2*p* derived states hybridized with Ba 5*d*, whereas E and F peaks indicated the transition from O 1*s* to O 2*p*-Ba 4*f* states (*52, 74*). The peaks were deconvoluted by fitting the O *K*-edge spectra with the Gaussian function and arctangent function as background. We note that the intensity of peak A (t_{2g}) dramatically decreased in Ni-substituted $BaTiO_3$ ceramics indicative of weakening of Ti 3*d* and O 2*p* hybridization by oxygen vacancy formation. Namely, the oxygen vacancy generation by Ni doping suppressed the polar Ti-O hybridization in tetragonal $BaTiO_3$ inducing a polymorphic transition to a 6H-hexagonal phase (*45,47*).

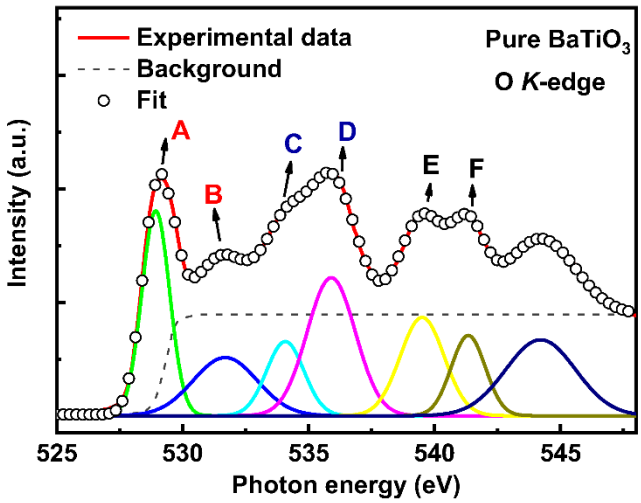

Fig. S1. The normalized O *K*-edge X-ray absorption spectra of pure $BaTiO_3$ ceramics. In O *K*-edge spectra, peaks A and B were attributed to the transition from O 1*s* to t_{2g} and e_g hybridized states between O 2*p*-Ti 3*d*, respectively. The features C and D were due to O 2*p* derived states hybridized with Ba 5*d*, whereas E and F peaks indicated the transition from O 1*s* to O 2*p*-Ba 4*f* states.

The simulated electron diffraction pattern of a 6H-hexagonal $BaTiO_3$

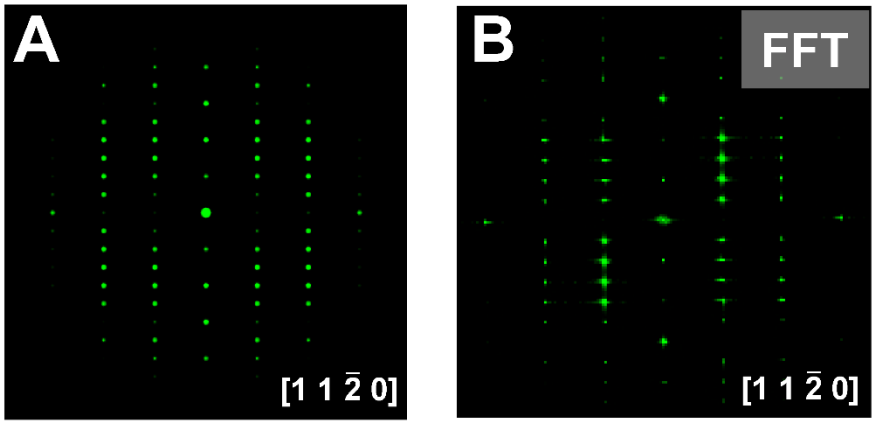

Fig. S2. The fast Fourier transform (FFT) analyses of Ni-substituted $BaTiO_3$ ceramics. (**A**) The simulated electron diffraction pattern of the 6H-hexagonal $BaTiO_3$ polymorph along [11$\bar{2}$0] direction. (**B**) The experimental FFT pattern of Ni-substituted $BaTiO_3$ ceramics.

Plots of frequency-dependent dielectric permittivity of pure $BaTiO_3$ ceramics at the as-sintered state and after a treatment by air exposure

To examine whether the dielectric responses of pure $BaTiO_3$ ceramics were affected by air exposure, we measured the frequency-dependent dielectric constant of pure ceramics at the as-sintered state and then, exposed the samples to the air environment at room temperature for 6 weeks. Next, we re-measured the dielectric responses of the treated pure $BaTiO_3$ ceramics. As shown in Fig. S3, there was no difference in the frequency-dependent dielectric permittivity data of pure $BaTiO_3$ ceramics, although the pure $BaTiO_3$ ceramics were treated via the 6-week-durational air exposure.

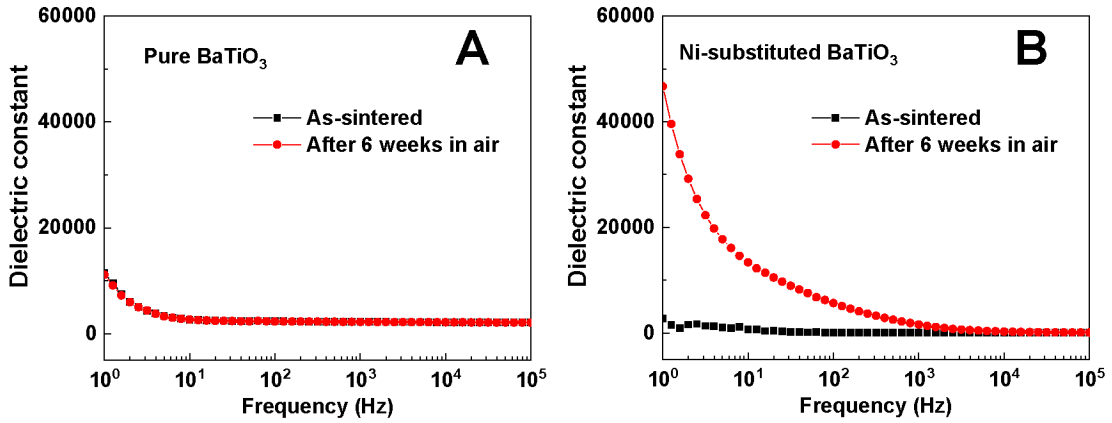

Fig. S3. The frequency-dependent dielectric permittivity of pure and Ni-substituted $BaTiO_3$ ceramics at the as-sintered state and after air exposure. The dielectric constant as a function of frequency in the (**A**) pure and (**B**) Ni-substituted $BaTiO_3$ ceramics at the as-sintered state (the black solid squares) and after 6 weeks in the ambient air (the red solid circles).

The effect of electric *dc* bias on dielectric responses

To investigate the effect of electric *dc* bias on dielectric responses of Ni-substituted $BaTiO_3$ ceramics, we designed a poling experiment, as shown in Fig. S4A. In detail, we carried out the frequency-dependent dielectric permittivity measurements in Ni-substituted $BaTiO_3$ ceramics at the as-sintered state (marked by B in Fig. S4A), after a treatment in the high-humidity environment (marked by C in Fig. S4A), and after a poling process (marked by D in Fig. S4A). It was evident that the as-sintered Ni-substituted $BaTiO_3$ ceramics exhibited the off-state in dielectric responses (Fig. S4B). When the ceramic samples were treated under the high humidity environment, the initial off-state in the as-sintered ceramics changed to the on-state in the treated ceramics (Fig. S4C). In the on-state (i.e., the treated ceramics by humidity), we poled the Ni-substituted $BaTiO_3$ capacitors by applying a *dc* voltage bias (V_s = 1 kV) during a time duration of t_s = 60 minutes. After poling the capacitors, we re-measured the dielectric permittivity as a function of frequency in the poled ceramics at room temperature.

Fig. S4D showed the frequency-dependent dielectric constant and loss of the poled ceramics. It was interesting that the dielectric permittivity in the low-frequency range dramatically decreased after a poling process. The high dielectric permittivity ($\varepsilon \sim 1.7\times10^7$ at 1 Hz) in the treated ceramics was reduced in the poled ceramics ($\varepsilon \sim 1.1\times10^4$ at 1 Hz) (Table S1). This indicated that the on-state in the treated ceramics was restored to the off-state by applying electrical *dc* bias.

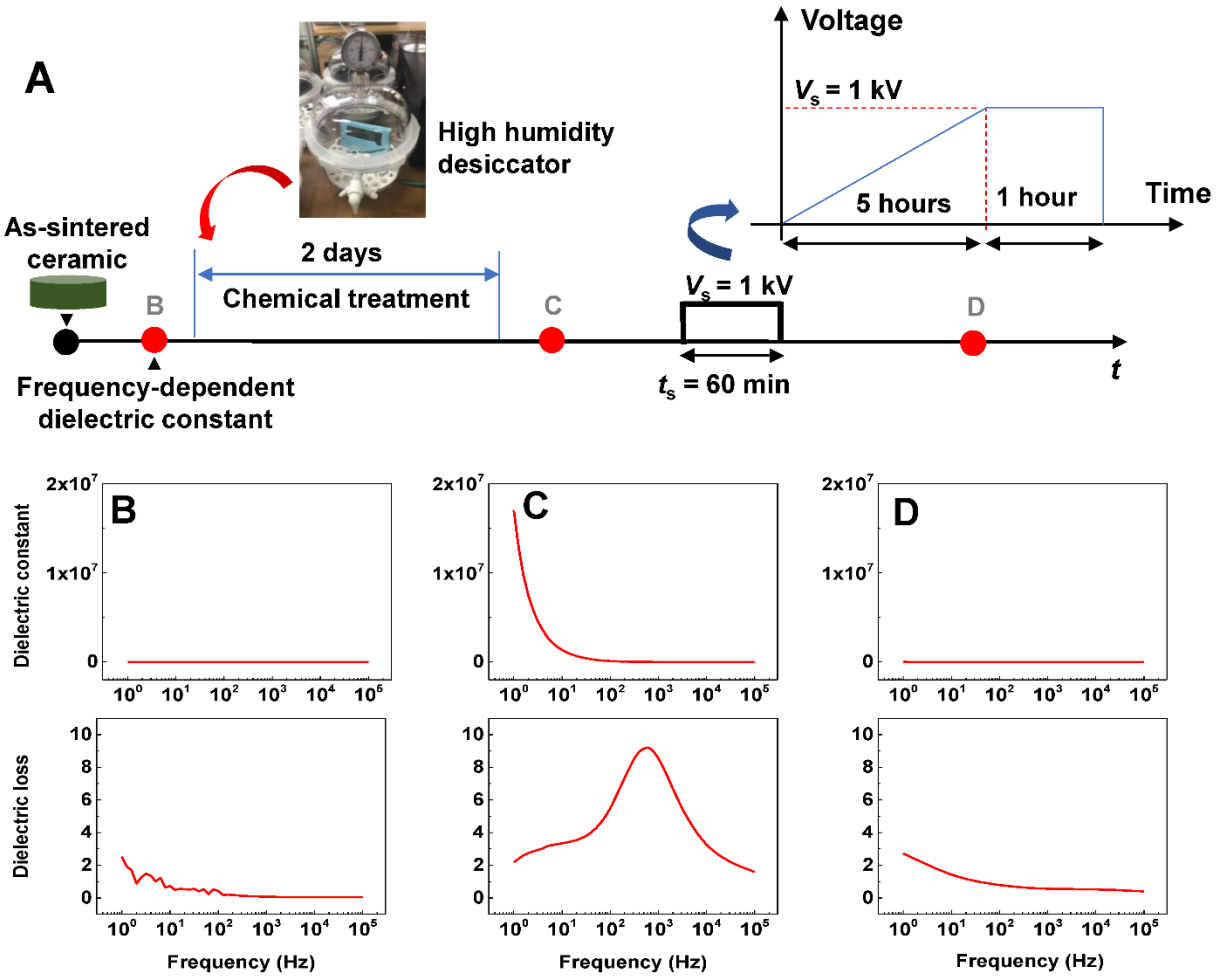

Fig. S4. The effect of electric *dc* bias on dielectric responses of Ni-substituted $BaTiO_3$ ceramics. (**A**) A schematic indicated the experimental sequence. (**B** to **D**) The frequency-dependent dielectric constant and loss of Ni-substituted $BaTiO_3$ ceramics (B) at the as-sintered state, (C) after the treatment in a humid environment, and (D) after the poling process.

Table S1. Dielectric constant values at 1 Hz in the ceramics at different states.

	As sintered	After treatment	After poling
ε at 1 Hz	2.8×10^3	1.7×10^7	1.1×10^4

The evolution of frequency-dependent dielectric constant in Ni-substituted $BaTiO_3$ ceramics under the ambient air environment

To track the evolution of the dielectric responses to the ambient air in Ni-substituted $BaTiO_3$ ceramics, we measured the frequency-dependent dielectric permittivity in the ceramic samples for different time duration of the air exposure. The frequency-dependent dielectric constant measurements were repeatedly performed in our ceramics with weekly time intervals (the experimental process in the schematic Fig. S5A). We observed that the dielectric permittivity in a low-frequency range (from 10^0 to 10^3 Hz) continuously increased with the increase of time duration (Fig. S5B). In particular, the dielectric constant ($\varepsilon \sim 2.5\times10^3$ at 1 Hz) in the as-sintered ceramics was enhanced up to the value of $\varepsilon \sim 4.6\times10^4$ after 6 weeks in the ambient air. As shown in Fig. S5C, the corresponding dielectric loss also increased after a treatment under the air environment. We plotted the dielectric constant values at 1 Hz as a function of the air-exposure time (Fig. S5D). For the first two weeks, the dielectric constant varied around the finite value of $\varepsilon \sim 2.7\times10^3$. After two weeks, the dielectric permittivity started to increase dramatically and then, it reached a high value of $\varepsilon \sim 4.6\times10^4$ after a time duration of 6 weeks.

We reset the on-state in the treated ceramics by air exposure to the initial off-state by thermal annealing, as shown in Fig. S5A. The high dielectric constant in the low-frequency region returned to a low value (black solid squares in Fig. S5E), while the dielectric loss also became reduced after thermal annealing (black solid squares in Fig. S5F). Then, we plotted the frequency-dependent dielectric constant and loss in the annealed ceramics as a function of the air-exposure time. Interestingly, the dielectric responses in the low-frequency region significantly increased after air exposure (Fig. S5E). The observed peak in the dielectric loss shifted to a higher frequency with the increase of the time duration (Fig. S5F). As shown in Fig. S5G, the dielectric permittivity kept increasing over the time and an extremely high dielectric constant ($\varepsilon \sim 6.9\times10^4$ at 1 Hz) was achieved after 6 weeks.

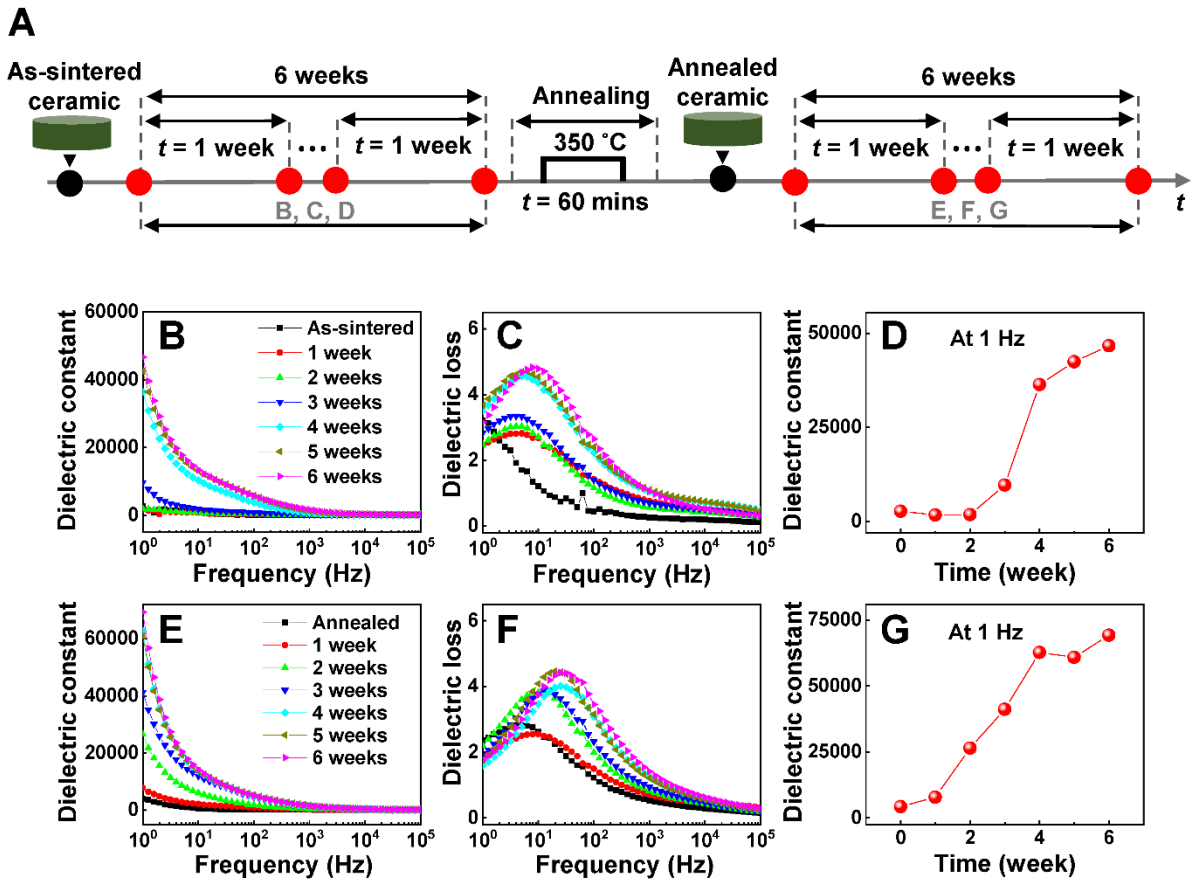

Fig. S5. The time-dependent evolution of dielectric responses in Ni-substituted $BaTiO_3$ ceramics under the ambient air environment. (**A**) A schematic of the experimental sequence. (**B**) The frequency-dependent dielectric permittivity in Ni-substituted $BaTiO_3$ ceramics for different time duration under the ambient air environment. (**C**) The corresponding dielectric loss as a function of frequency for different time duration of the air exposure. (**D**) The dielectric constant as a function of time duration at 1 Hz in (B). (**E**) The dielectric constant and (**F**) dielectric loss as a function of frequency in the annealed ceramics for different time duration of the air exposure. (**G**) The air-exposure time dependence of dielectric permittivity at 1 Hz in (E).

Experimental set-up of Ni-substituted $BaTiO_3$ ceramics under vacuum, nitrogen, carbon dioxide, and high humidity environments

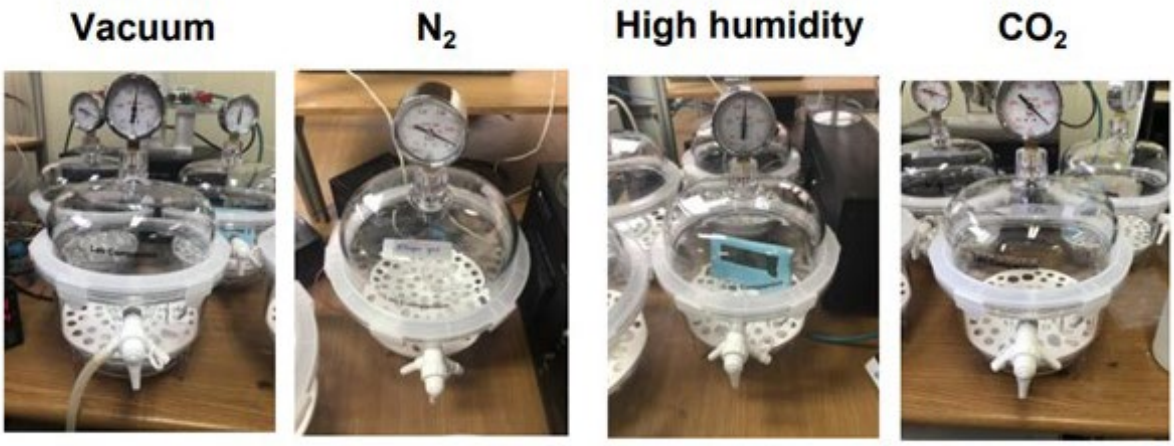

Fig. S6. Experimental set-up of Ni-substituted $BaTiO_3$ ceramics under vacuum, nitrogen (N_2), carbon dioxide (CO_2), and high humidity environments.

Table S2. Base pressure, time duration, and description of various ambient treatments.

Treatment	Base pressure	Time duration	Description
Vacuum	~380 Torr	1 week	The sample under a low vacuum of ~ 380 Torr
Nitrogen (N_2)	~380 Torr	1 week	The sample under ~ 700 Torr of N_2
Carbon dioxide (CO_2)	~380 Torr	1 week	The sample under ~ 700 Torr of CO_2
High humidity	~380 Torr	2 days	The sample under a low vacuum of ~ 380 Torr with distilled water at the bottom of the desiccator

A comparison of the achieved dielectric constant in our Ni-substituted $BaTiO_3$ ceramics with the colossal dielectric permittivity in several oxide ceramics reported in earlier studies

Table S3. The dielectric constant in the treated Ni-substituted $BaTiO_3$ ceramics under a humid condition and the colossal dielectric permittivity previously reported in various oxides ceramics.

Composition	Dielectric constant (ε)			Temperature	References
	At 1 Hz	At 10 Hz	At 100 Hz		
$Ba(Ti_{0.825}Ni_{0.175})O_{3-\delta}$	5.2×10^6	8.8×10^5	9.4×10^4	Room temperature	Current work
Previous works					
$CaCu_3Ti_4O_{12}$	1.0×10^6	5.0×10^5	3.0×10^5	308 K	(*75*)
$(In_{0.5}Nb_{0.5})_{0.01}Ti_{0.99}O_2$	1.0×10^7	1.0×10^6	2.0×10^5	Room temperature	(*76*)
$(Al_{0.5}Nb_{0.5})_{0.3}Ti_{0.7}O_2$	1.4×10^5	1.2×10^5	1.0×10^5	Room temperature	(*77*)

Change of dielectric responses in Ni-substituted $BaTiO_3$ ceramics by water treatment

To further verify the effect of water molecules on the dielectric properties of Ni-substituted $BaTiO_3$ ceramics, a water-treatment experiment was conducted (see Fig. S7A). As shown in Figs. S7B and S7C, we measured the dielectric permittivity and dielectric loss in Ni-substituted $BaTiO_3$ ceramics before (black squares) and after (red circles) the water treatment. We found that the off-state immediately changed to the on-state after a short time duration (t ~ 10 minutes) of the water treatment. For a comparison, we also carried out the water-treatment experiment of pure $BaTiO_3$ ceramics. The dielectric responses of pure ceramics were almost unchanged before (black squares) and after (red circles) the water treatment (Figs. S7D and S7E). It was clear that a change in dielectric responses induced by the water treatment only emerged in for the Ni-substituted $BaTiO_3$ ceramics, not pure $BaTiO_3$.

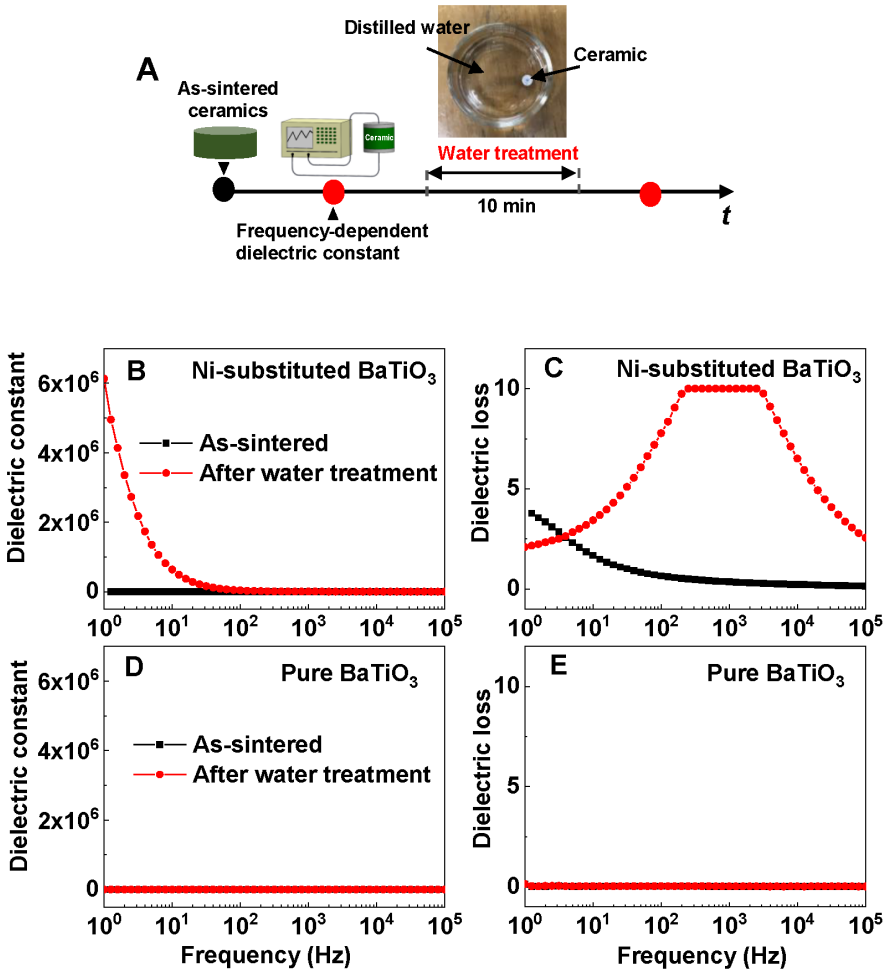

Fig. S7. Change of dielectric constant in Ni-substituted $BaTiO_3$ ceramics induced by water treatment. (**A**) The sequence of the water-treatment experiment. We measured the dielectric properties of ceramic samples before and after the water treatment. (**B**) The dielectric constant and (**C**) the dielectric loss in Ni-substituted $BaTiO_3$ ceramics at the as-sintered state and after the water treatment. (**D**) The dielectric constant and (**E**) the dielectric loss of the pure $BaTiO_3$ ceramics at the as-sintered state and after the water treatment.

Electrical resistance in pure $BaTiO_3$ ceramics at different relative-humidity levels

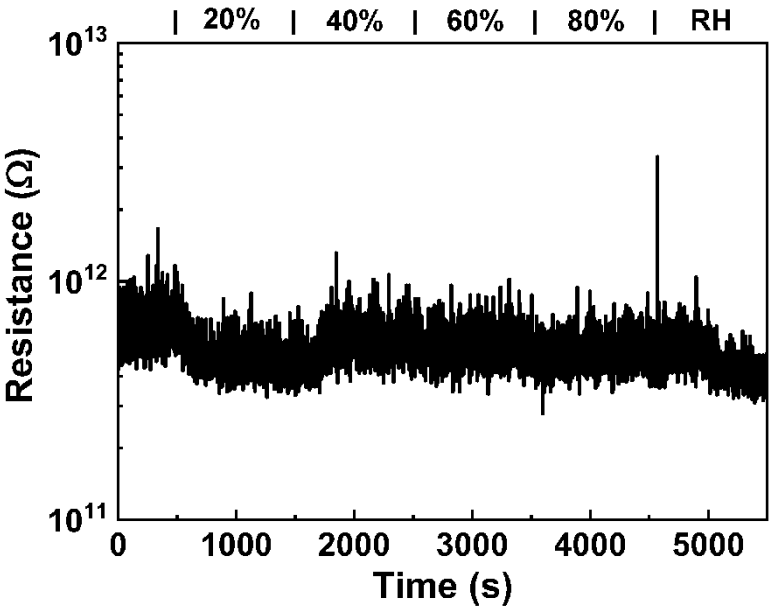

Fig. S8. Evolution of the resistance of pure $BaTiO_3$ ceramics as a function of the relative humidity.

Impedance analyses for the off- and on-states at various temperatures

We carried out the impedance measurements to ceramics with the on- and off-states for different temperatures (varying from 20 to 180 ˚C). We also deconvoluted our impedance data to the semicircular arcs. Note that each semicircular arc in impedance spectra represented a dielectric relaxation characteristic arising from a parallel electrical circuit between one capacitor and one resistor. As shown in Fig. S9, the observed impedance spectra at various temperatures for the off-state were almost fitted for a single semicircular arc. It was plausible that the majority of electrical currents passed through the grain boundaries in the off-state where the accumulated oxygen vacancies at grain boundaries acted as a conducting channel (*78*). In contrast, the impedance responses of the on-state showed that electrical currents went through both grains and grain boundaries resulting in the double-semicircular curve (Fig. S10) (*78*).

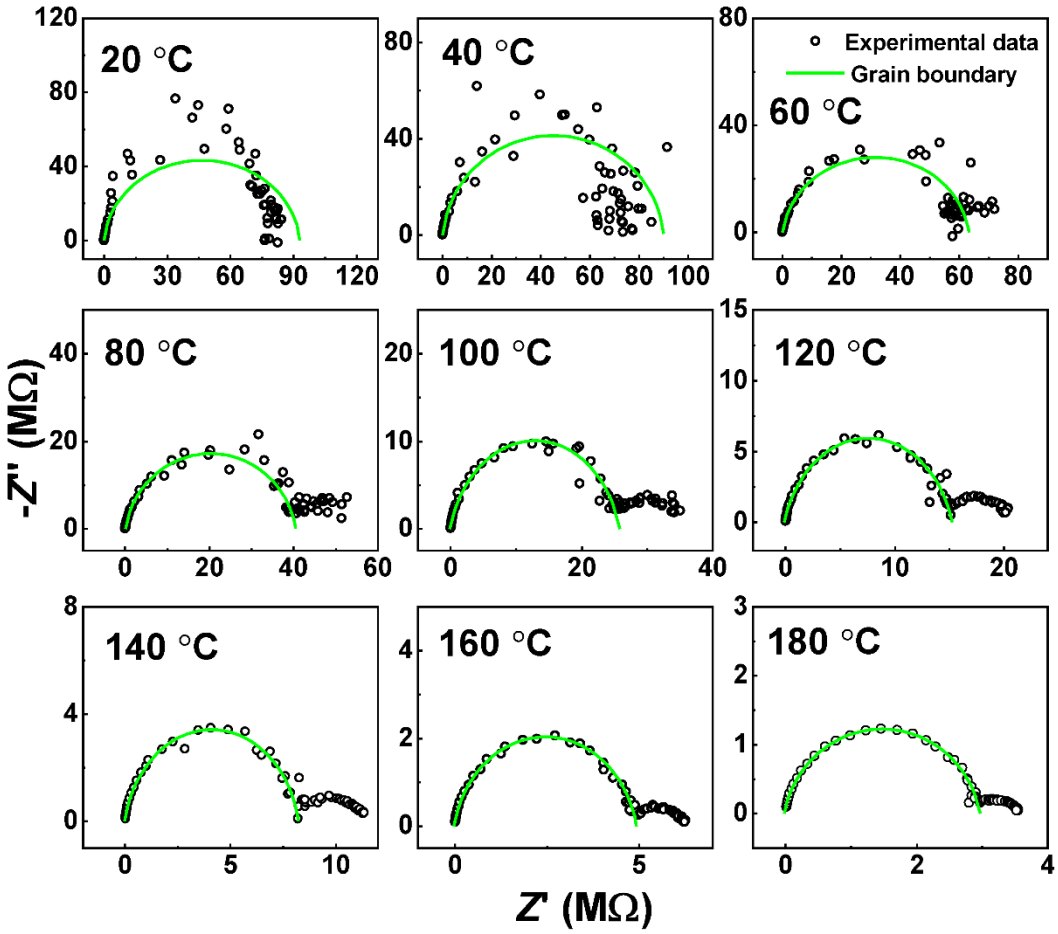

Fig. S9. The impedance Cole-Cole plots in Ni-substituted $BaTiO_3$ ceramics at various temperatures for the off-state.

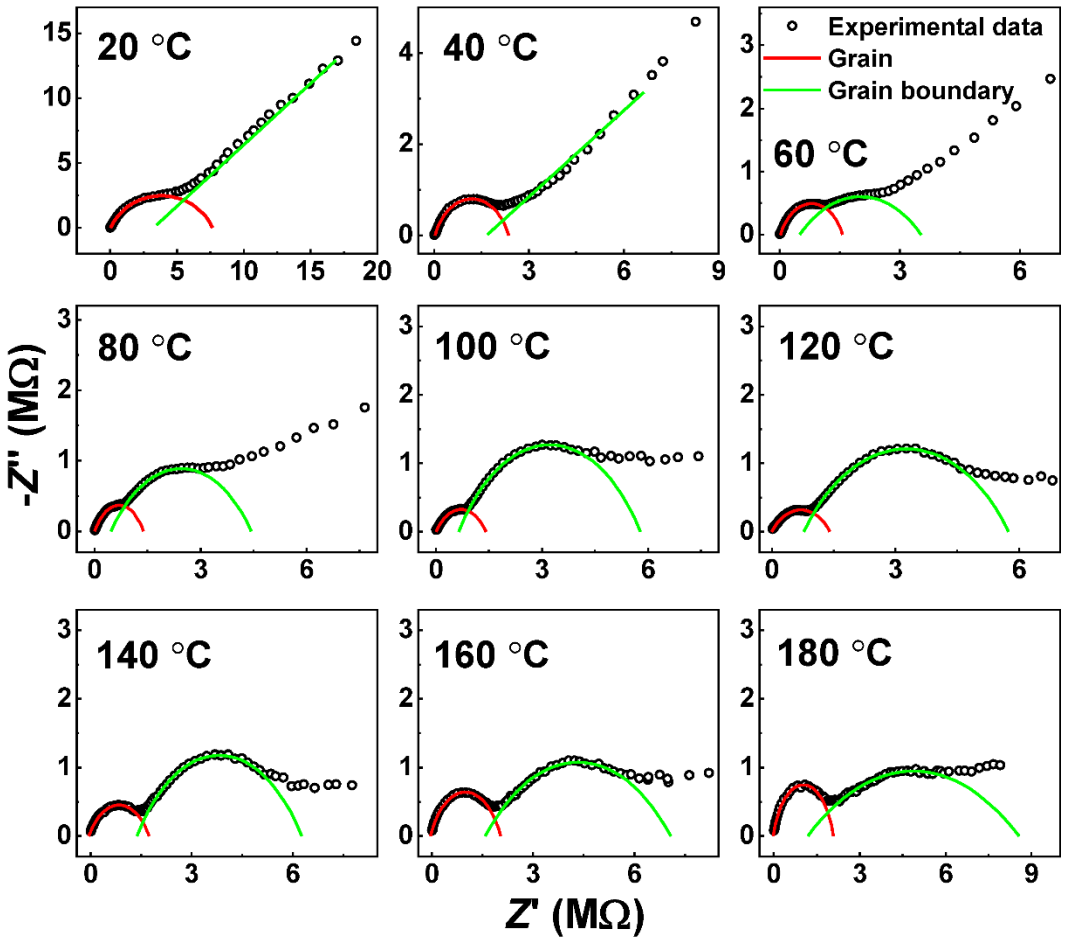

Fig. S10. The impedance Cole-Cole plots in Ni-substituted $BaTiO_3$ ceramics at various temperatures for the on-state.

X-ray photoelectron spectroscopy (XPS) measurements

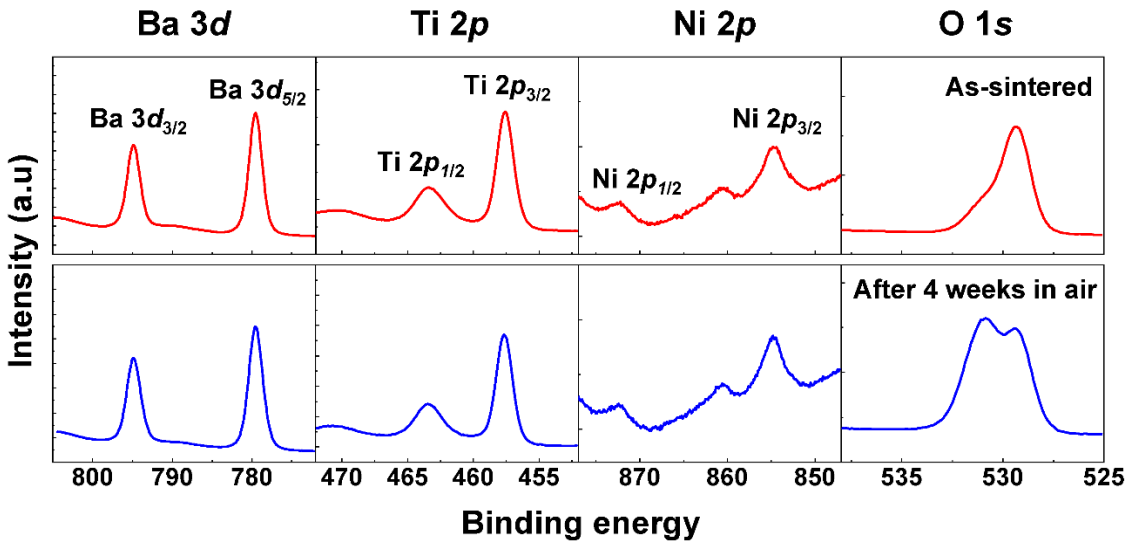

Fig. S11. XPS spectra of Ba 3*d*, Ti 2*p*, Ni 2*p*, and O 1*s* edges of Ni-substituted $BaTiO_3$ ceramics at the as-sintered state (red solid curves) and after air exposure for 4 weeks (blue solid curves).

The field emission-scanning electron microscope (FE-SEM) and energy dispersive spectroscopy (EDS) analyses

Fig. S12 showed the field emission-scanning electron microscope (FE-SEM) images and corresponding energy dispersive spectroscopy (EDS) results of the as-sintered Ni-substituted $BaTiO_3$ ceramics. We visualized the spatial distribution of each element for grains (i.e., area indicated by red polygons in Figs. S12A and S12B) and grain boundaries (i.e., red solid lines in Figs. S12A and S12B). The corresponding EDS mapping data at Ba *L*-, Ti *K*-, and Ni *K*-edges showed the uniform contribution of elements. In contrast, there was an inhomogeneous distribution of the oxygen element in O *K*-edge spectra. From local EDS measurements (Fig. S13), the atomic percentages of the oxygen element were 74.8 and 50.2% at grains and grain boundaries in the as-sintered ceramics, respectively. This indicated that the grain boundary regions were significantly oxygen-deficient compared with the grain regions.

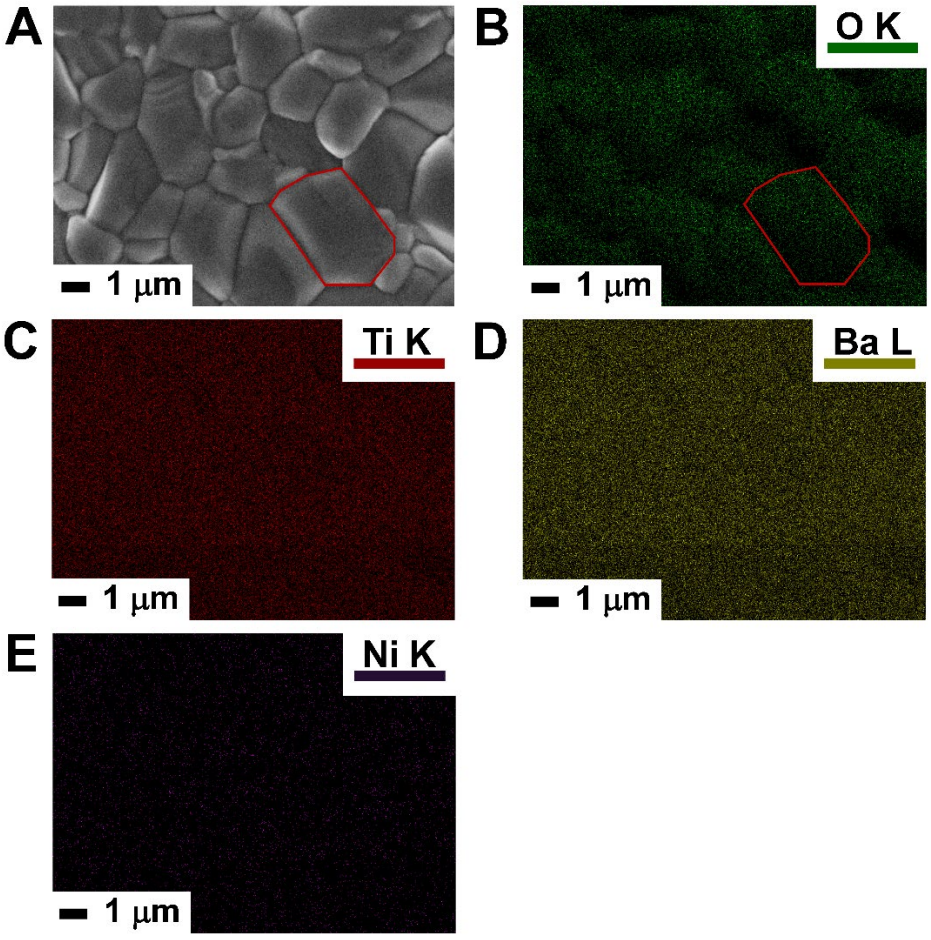

Fig. S12. Surface morphology and elemental mapping analyses of the as-sintered Ni-substituted $BaTiO_3$ ceramics. (**A**) The field emission-scanning electron microscopy (FE-SEM) surface image of the as-sintered Ni-substituted $BaTiO_3$ ceramics. (**B** to **E**) The corresponding EDS mapping data of O, Ti, Ba, and Ni elements on the ceramic surface in (A), respectively. Area inside the red polygons in the FE-SEM image (A) and the O *K*-edge spectrum (B) represented grains.

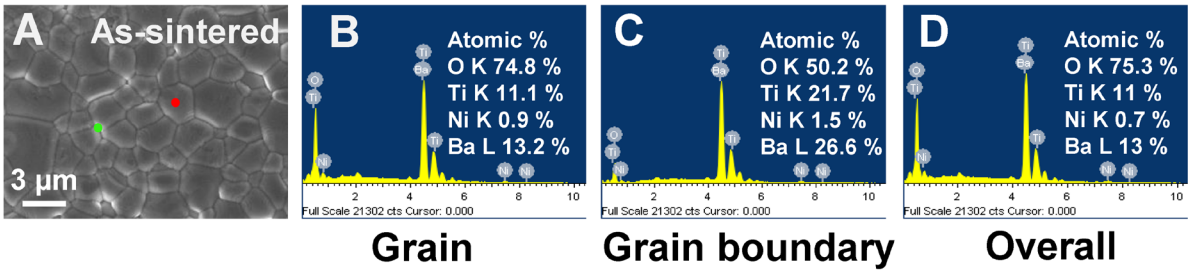

Fig. S13. The EDS analyses of the as-sintered Ni-substituted $BaTiO_3$ ceramics in grains and grain boundaries. (**A**) The field emission-scanning electron microscopy (FE-SEM) image of the as-sintered Ni-substituted $BaTiO_3$ ceramics. (**B** and **C**) The local EDS spectra of (B) a grain [marked by the red spot in (A)] and (C) a grain boundary [marked by the green spot in (A)]. (**D**) The averaged EDS spectrum on the sample surface of (A).

Possible explanations of a change in dielectric responses induced by air exposure

For the as-sintered state, the oxygen vacancy defects in Ni-substituted $BaTiO_3$ ceramics were mostly accumulated in the proximity of grain boundaries (Fig. S14A). The as-sintered ceramics exhibited a low dielectric constant throughout the whole frequency range with slight variations. Owing to the accumulation of oxygen vacancies at grain boundaries, the grain boundary regions became more conductive than grain regions in ceramics. Thus, the electrical circuit of the as-sintered Ni-substituted $BaTiO_3$ ceramics was equivalent to the parallel circuit of the resistance (R) and capacitance (C) of the grain boundary component. When the Ni-substituted $BaTiO_3$ ceramics were exposed to air, the hydroxyl ions dissociated from the water were adsorbed on oxygen vacancies nearby the grain boundaries (Fig. S14B). On the other hand, dissociated protons (H^+) could be introduced into grains of ceramics (Fig. S14C). The introduction of protons with a positive charge inside ceramics modified the overall dielectric responses in the Ni-substituted $BaTiO_3$ ceramics. After air exposure, the Ni-substituted $BaTiO_3$ ceramics showed dielectric relaxation behaviors with the increasing frequency and an ultrahigh dielectric constant was achieved at a low frequency. The equivalent circuit model of the Ni-substituted $BaTiO_3$ ceramics after air exposure corresponded to a series of two R-C parallel connections for both the grain and grain boundary components, respectively.

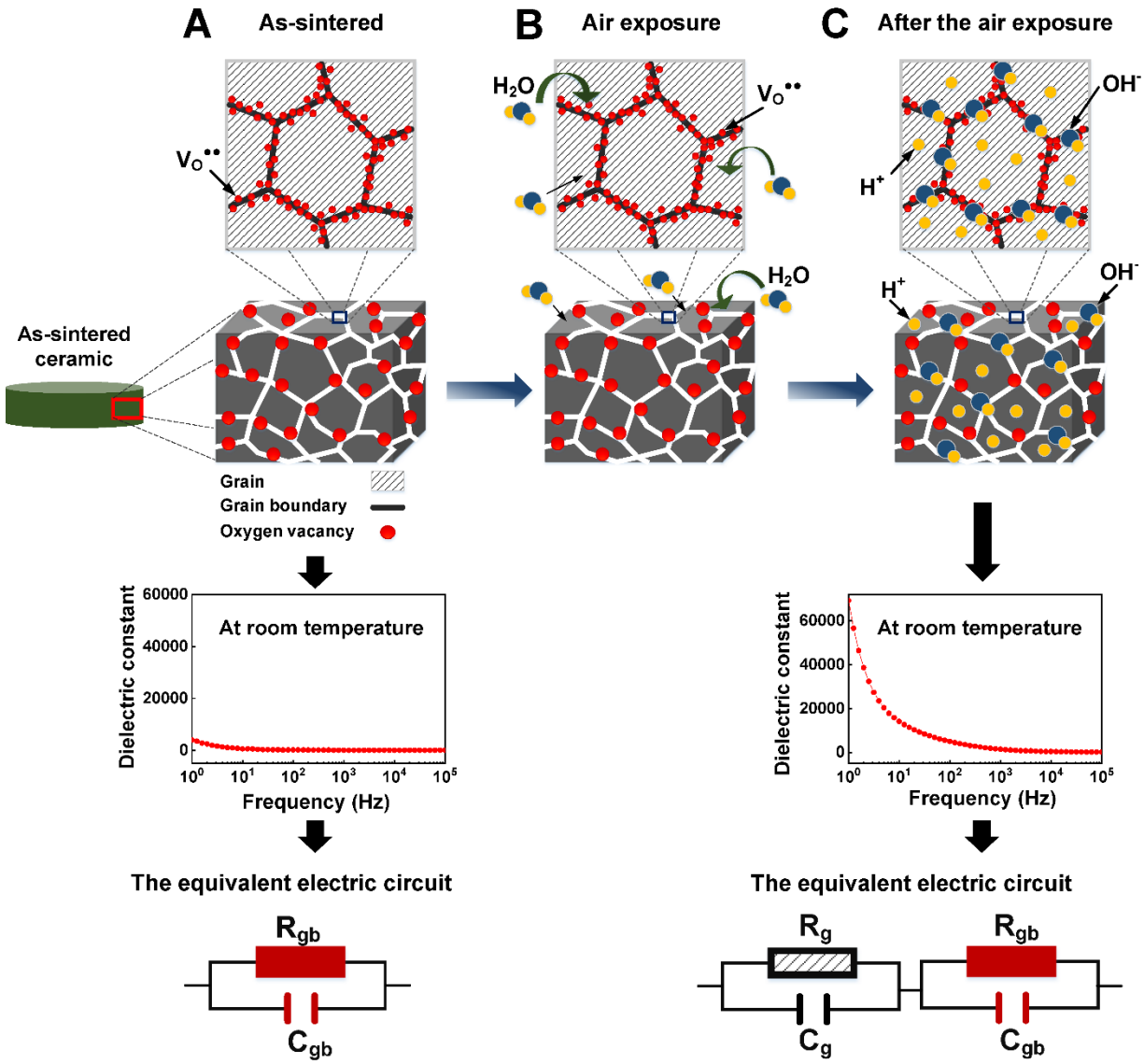

Fig. S14. The schematic illustration of a change in dielectric responses of Ni-substituted $BaTiO_3$ ceramics under the ambient air environment. (**A**) For the as-sintered state, most oxygen vacancies were accumulated at grain boundaries. The electrical circuit was equivalent to a parallel circuit of the resistance (*R*) and capacitance (*C*) for the grain boundary component. (**B**) The Ni-substituted $BaTiO_3$ ceramics were exposed to the ambient air. (**C**) Hydroxyl ions dissociated water molecules were adsorbed at oxygen vacancy sites on the surface, while hydrogen ions were introduced to ceramics. For the ceramics after air exposure, the equivalent electrical circuit was a series of two *R*-*C* parallel connections for both the grain and grain boundary components.

Conductive atomic force microscopy (c-AFM) measurements

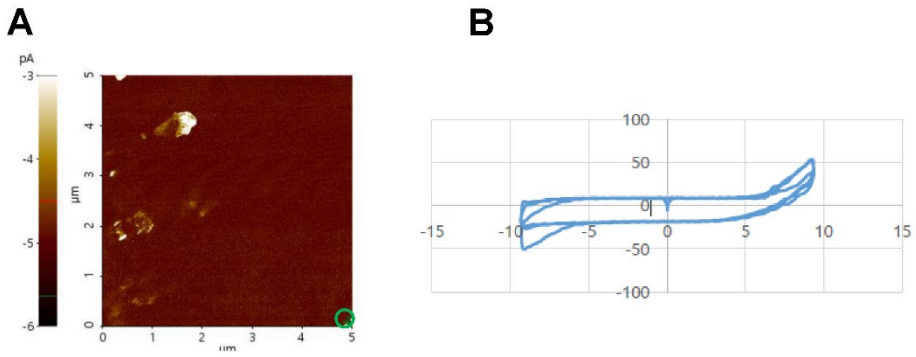

Fig. S15. Conductive atomic force microscopy (c-AFM) analyses of Ni-substituted $BaTiO_3$ ceramics for the on-state. (**A**) The c-AFM current map at 5 V bias voltage in Ni-substituted $BaTiO_3$ ceramics for the on-state. (**B**) The corresponding local *I-V* curve at the position marked by a green circle in (A).

An experimental set-up of acetic acid treatments

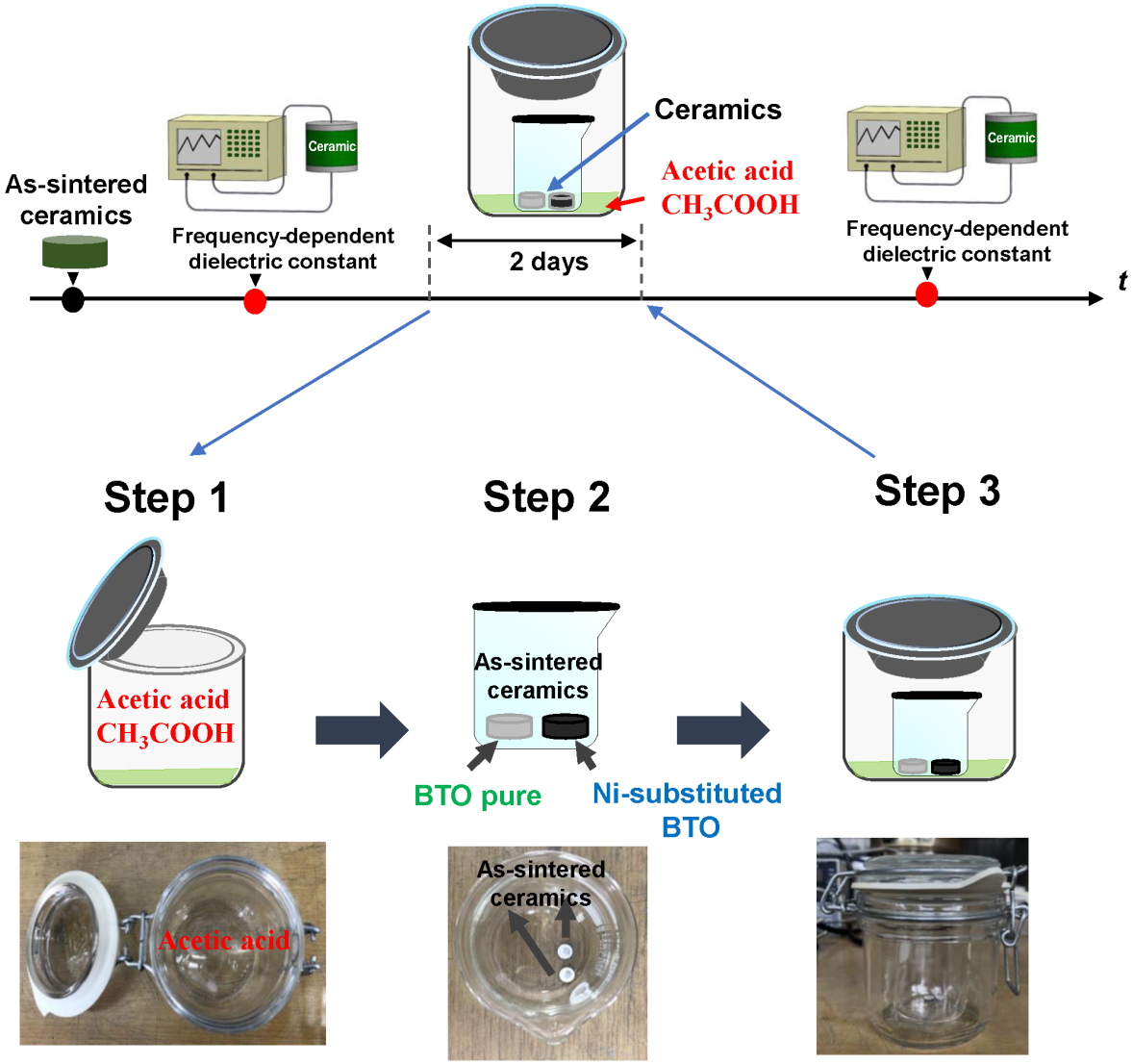

Fig. S16. A schematic represented the experimental set-up of the acid acetic treatment. The top/bottom sides of the pure and Ni-substituted $BaTiO_3$ ceramics were coated by silver pastes for the as-sintered state and then, we measured the frequency-dependent dielectric permittivity of the silver-coated ceramics. Next, we inserted a few droplets of acetic acid (CH_3COOH, 99.7%, Sigma-Aldrich, USA) into the bottom of a glass jar (Step 1). We put the pure and Ni-substituted $BaTiO_3$ ceramics in another beaker (Step 2 in the schematic). Then, the beaker with the ceramic samples was placed inside the jar to separate the ceramics from the acid liquid. The glass jar was closed, and the ceramics remained under the acid acetic-rich environment (Step 3). After 2 days, we took the ceramics out of the jar and re-measured the dielectric properties.

Change of dielectric responses in Ni-substituted $BaTiO_3$ ceramics by acetic acid treatment

Another route to modify the dielectric responses in Ni-substituted $BaTiO_3$ ceramics was an acetic acid (CH_3COOH) treatment. The experimental procedures of our acetic acid treatments were depicted in Fig. S16. Before the acetic acid treatments, the dielectric behaviors corresponded to the off-state (Fig. S17A). As shown in Fig. S17B, the low-frequency dielectric constant was dramatically enhanced by the acetic acid treatments. For the treated ceramic samples, we observed the extremely high dielectric permittivity ($\varepsilon \sim 10^6$ at 1Hz) which was three orders of magnitude larger that the initial value. We also identified that the dielectric constant rapidly decreased, when the sample was exposed to the ambient air after the acetic acid treatment (Fig. S17B). By plotting the dielectric constant as a function of the air-exposure time, we found that the dielectric permittivity continuously decreased over the time (Fig. S17C). Unlike the Ni-substituted $BaTiO_3$ ceramics, the dielectric responses in pure $BaTiO_3$ ceramics were almost unchanged before and after the acetic acid treatment (Fig. S17, D to F).

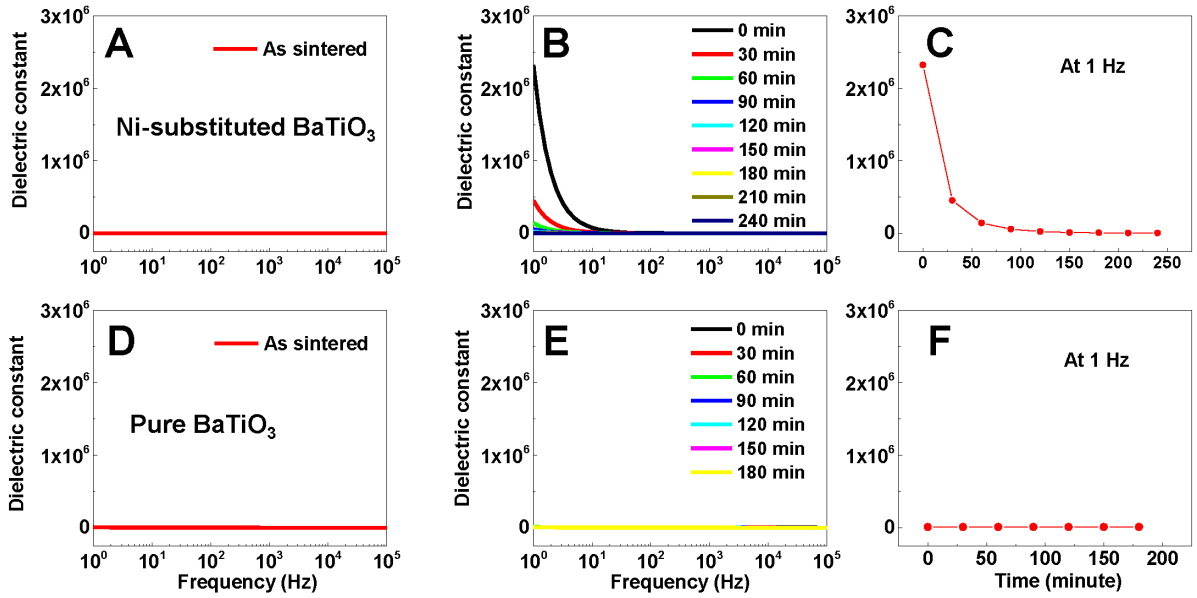

Fig. S17. The evolution of dielectric responses in Ni-substituted and pure $BaTiO_3$ ceramics by acetic acid treatments. (**A** and **D**) The dielectric constants as a function of frequency in (A) Ni-substituted and (D) pure $BaTiO_3$ ceramics for the as-sintered states. After a two-day treatment in the acetic acid environment, we re-measured the dielectric constants of the treated ceramics in the air. (**B** and **E**) The frequency dependences of dielectric constants in (B) Ni-substituted and (E) pure ceramics for various time duration of the exposure to ambient air. (**C** and **F**) The air-exposure time dependences of dielectric permittivity at 1 Hz in (B) and (E).

X-ray diffraction (XRD) patterns of Ni-substituted $BaTiO_3$ ceramics for the on- and off-states

We identified the crystal structure of the as-sintered (off-state) and the treated (on-state attained by a treatment under a humid environment) Ni-substituted $BaTiO_3$ ceramics using X-ray diffraction (XRD) analyses. To examine the dielectric properties, we first deposited the Pt electrodes on the top and bottom sides of the as-sintered ceramic pellets. Then, the XRD and frequency-dependent dielectric permittivity measurements were performed in the as-sintered ceramics, respectively (Figs. S18A and S18B). Next, the as-sintered ceramics were treated under a humidity condition for two days. After the high-humidity treatment, we repeated the measurements of XRD data and frequency-dependent dielectric constant in the treated ceramics (Figs. S18A and S18B). The diffraction patterns of the off-state (i.e., the as-sintered ceramics) and on-state (i.e., the treated ceramics) were consistent with the reference XRD pattern of a hexagonal structure (marked by the blue bar in Figs. S18A and S18C) (*45*). Note that the diffraction peaks at 2θ angles of 39.5 and 45.6° were attributed to the Pt metal electrodes [marked by asterisks (∗) in Figs. S18A and S18C]. The as-sintered and treated ceramics were structurally 6H-hexagonal for both off- and on-states, which indicated that the change of dielectric responses in the Ni-substituted $BaTiO_3$ ceramics would not originate from a structural phase transition.

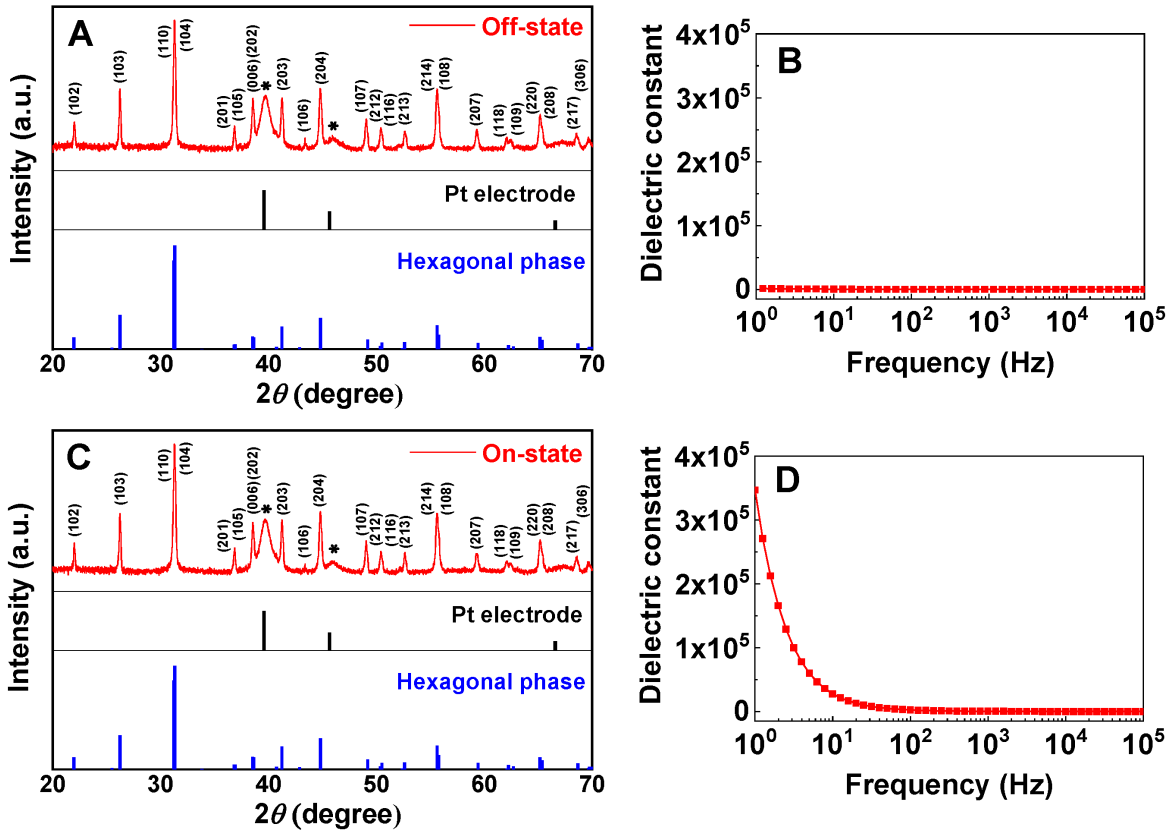

Fig. S18. X-ray diffraction (XRD) analyses of dielectric off- and on-states. The XRD patterns of Ni-substituted $BaTiO_3$ ceramics for (**A**) the off- and (**C**) on-states. The corresponding frequency-dependent dielectric constants of (**B**) the off- and (**D**) on-states.

REFERENCES AND NOTES

1. J.-K. Huang, Y. Wan, J. Shi, J. Zhang, Z. Wang, W. Wang, N. Yang, Y. Liu, C.-H. Lin, X. Guan, L. Hu, Z.-L. Yang, B.-C. Huang, Y.-P. Chiu, J. Yang, V. Tung, D. Wang, K. Kalantar-Zadeh, T. Wu, X. Zu, L. Qiao, L.-J. Li, S. Li, High-κ perovskite membranes as insulators for two-dimensional transistors. *Nature* **605**, 262–267 (2022).

2. A. I. Kingon, J.-P. Maria, S. K. Streiffer, Alternative dielectrics to silicon dioxide for memory and logic devices. *Nature* **406**, 1032–1038 (2000).

3. S. Krohns, P. Lunkenheimer, S. Meissner, A. Reller, B. Gleich, A. Rathgeber, T. Gaugler, H. U. Buhl, D. C. Sinclair, A. Loidl, The route to resource-efficient novel materials. *Nat. Mater.* **10**, 899–901 (2011).

4. S. C. B. Mannsfeld, B. C. K. Tee, R. M. Stoltenberg, C. V. Chen, S. Barman, B. V. O. Muir, A. N. Sokolov, C. Reese, Z. Bao, Highly sensitive flexible pressure sensors with microstructured rubber dielectric layers. *Nat. Mater.* **9**, 859–864 (2010).

5. W. H. Ko, Q. Wang, Touch mode capacitive pressure sensors. *Sens. Actuator A Phys.* **75**, 242–251 (1999).

6. M. Acosta, N. Novak, V. Rojas, S. Patel, R. Vaish, J. Koruza, G. Rossetti Jr., J. Rödel, $BaTiO_3$-based piezoelectrics: Fundamentals, current status, and perspectives. *Appl. Phys. Rev.* **4**, 041305 (2017).

7. M. E. Lines, A. M. Glass, *Principles and Applications of Ferroelectrics and Related Materials* (Oxford Classic Text in the Physical Sciences, Oxford Univ. Press, 2001).

8. B. Jaffe, W. Cook, H. Jaffe, *Piezoelectric Ceramics* (Academic, 1971).

9. M. Dawber, K. M. Rabe, J. F. Scott, Physics of thin-film ferroelectric oxides. *Rev. Mod. Phys.* **77**, 1083–1130 (2005).

10. M. Arshad, H. Du, M. S. Javed, A. Maqsood, I. Ashraf, S. Hussain, W. Ma, H. Ran, Fabrication, structure, and frequency-dependent electrical and dielectric properties of Sr-doped $BaTiO_3$ ceramics. *Ceram. Int.* **46**, 2238–2246 (2020).

11. G. Wang, C. Wang, S. Huang, C. Lei, X. Sun, T. Li, L. Liu, Origin of colossal dielectric behavior in double perovskite Ba_2CoNbO_6. *J. Am. Ceram. Soc.* **96**, 2203–2210 (2013).

12. W. Z. Yang, M. S. Fu, X. Q. Liu, H. Y. Zhu, X. M. Chen, Giant dielectric response and mixed-valent structure in the layered-ordered double-perovskite ceramics. *Ceram. Int.* **37**, 2747–2753 (2011).

13. W. Hu, Y. Liu, R. L. Withers, T. J. Frankcombe, L. Norén, A. Snashall, M. Kitchin, P. Smith, B. Gong, H. Chen, S. Jason, F. Brink, J. Wong-Leung, Electron-pinned defect-dipoles for high-performance colossal permittivity materials. *Nat. Mater.* **12**, 821–826 (2013).

14. Y. Song, X. Wang, Y. Sui, Z. Liu, Y. Zhang, H. Zhan, B. Song, Z. Liu, Z. Lv, L. Tao, J. Tang, Origin of colossal dielectric permittivity of rutile $Ti_{0.9}In_{0.05}Nb_{0.05}O_2$: Single crystal and polycrystalline. *Sci. Rep.* **6**, 21478 (2016).

15. H. Han, C. Voisin, S. Guillemet-Fritsch, P. Dufour, C. Tenailleau, C. Turner, J. C. Nino, Origin of colossal permittivity in $BaTiO_3$ via broadband dielectric spectroscopy. *J. Appl. Phys.* **113**, 024102 (2013).

16. S. Guillemet-Fritsch, Z. Valdez-Nava, C. Tenailleau, T. Lebey, B. Durand, J.-Y. Chane-Ching, Colossal permittivity in ultrafine grain size $BaTiO_{3-x}$ and $Ba_{0.95}La_{0.05}TiO_{3-x}$ materials. *Adv. Mater.* **20**, 551–555 (2008).

17. C. C. Homes, T. Vogt, S. M. Shapiro, S. Wakimoto, A. P. Ramirez, Optical response of high-dielectric-constant perovskite-related oxide. *Science* **293**, 673–676 (2001).

18. M. A. Subramanian, D. Li, N. Duan, B. A. Reisner, A. W. Sleight, High dielectric constant in $ACu_3Ti_4O_{12}$ and $ACu_3Ti_3FeO_{12}$ phases. *J. Solid State Chem.* **151**, 323–325 (2000).

19. A. P. Ramirez, M. A. Subramanian, M. Gardel, G. Blumberg, D. Li, T. Vogt, S. M. Shapiro, Giant dielectric constant response in a copper-titanate. *Solid State Commun.* **115**, 217–220 (2000).

20. P. Lunkenheimer, R. Fichtl, S. G. Ebbinghaus, A. Loidl, Nonintrinsic origin of the colossal dielectric constants $_{in}CaCu_3Ti_4O_{12}$. *Phys. Rev. B* **70**, 172102 (2004).

21. P. Lunkenheimer, V. Bobnar, A. V. Pronin, A. I. Ritus, A. A. Volkov, A. Loidl, Origin of apparent colossal dielectric constants. *Phys. Rev. B* **66**, 052105 (2002).

22. D. C. Sinclair, T. B. Adams, F. D. Morrison, A. R. West, $CaCu_3Ti_4O_{12}$: One-step internal barrier layer capacitor. *Appl. Phys. Lett.* **80**, 2153–2155 (2002).

23. M. Li, X. L. Chen, D. F. Zhang, W. Y. Wang, W. J. Wang, Humidity sensitive properties of pure and Mg-doped $CaCu_3Ti_4O_{12}$. *Sens. Actuators B Chem.* **147**, 447–452 (2010).

24. B. M. Kulwicki, Humidity sensors. *J. Am. Ceram. Soc.* **74**, 697–708 (1991).

25. S. Wan, H. Bi, Y. Zhou, X. Xie, S. Su, K. Yin, L. Sun, Graphene oxide as high-performance dielectric materials for capacitive pressure sensors. *Carbon* **114**, 209–216 (2017).

26. X. Liu, S. Cheng, H. Liu, S. Hu, D. Zhang, H. Ning, A survey on gas sensing technology. *Sensors* **12**, 9635–9665 (2012).

27. A. Dey, Semiconductor metal oxide gas sensors: A review. *Mater. Sci. Eng. B* **229**, 206–217 (2018).

28. P. M. Harrey, B. J. Ramsey, P. S. A. Evans, D. J. Harrison, Capacitive-type humidity sensors fabricated using the offset lithographic printing process. *Sens. Actuators B Chem.* **87**, 226–232 (2002).

29. T. Ishihara, S. Matsubara, Capacitive type gas sensors. *J. Electroceramics* **2**, 215–228 (1998).

30. W. C. Wang, Y. T. Tian, K. Li, E. Y. Lu, D. S. Gong, X. J. Li, Capacitive humidity-sensing properties of Zn_2SiO_4 film grown on silicon nanoporous pillar array. *Appl. Surf. Sci.* **273**, 372–376 (2013).

31. P. Bindra, A. Hazra, Selective detection of organic vapors using TiO_2 nanotubes based single sensor at room temperature. *Sens. Actuators B Chem.* **290**, 684–690 (2019).

32. H. Bi, K. Yin, X. Xie, J. Ji, S. Wan, L. Sun, M. Terrones, M. S. Dresselhaus, Ultrahigh humidity sensitivity of graphene oxide. *Sci. Rep.* **3**, 2714 (2013).

33. D. M. Pozar, *Microwave Engineering* (Wiley, 2011).

34. K. C. Kao, *Dielectric Phenomena in Solids* (Elsevier, 2004).

35. H. Yoon, M. Choi, T.-W. Lim, H. Kwon, K. Ihm, J. K. Kim, S.-Y. Choi, J. Son, Reversible phase modulation and hydrogen storage in multivalent VO_2 epitaxial thin films. *Nat. Mater.* **15**, 1113–1119 (2016).

36. A. Janotti, C. G. Van de Walle, Hydrogen multicentre bonds. *Nat. Mater.* **6**, 44–47 (2007).

37. S. Shen, Z. Li, Z. Tian, W. Luo, S. Okamoto, P. Yu, Emergent Ferromagnetism with Fermi-Liquid Behavior in Proton $_{\text{Intercalated}}CaRuO_3$. *Phys. Rev. X* **11**, 021018 (2021).

38. R. D. Shannon, Revised effective ionic radii and systematic studies of interatomic distances in halides and chalcogenides. *Acta Crystallogr. A* **32**, 751–767 (1976).

39. C. Amsler, M. Doser, M. Antonelli, D. M. Asner, K. S. Babu, H. Baer, H. R. Band, R. M. Barnett, E. Bergren, J. Beringer, G. Bernardi, W. Bertl, H. Bichsel, O. Biebel, P. Bloch, E. Blucher, S. Blusk, R. N. Cahn, M. Carena, C. C. A. Ceccucci, D. Chakraborty, M. C. Chen, R. S. Chivukula, G. Cowan, O. Dahl, G. D'Ambrosio, T. Damour, A. de Gouvêa, T. DeGrand, B. Dobrescu, M. Drees, D. A. Edwards, S. Eidelman, V. D. Elvira, J. Erler, V. V. Ezhela, J. L. Feng, W. Fetscher, B. D. Fields, B. Foster, T. K. Gaisser, L. Garren, H. J. Gerber, G. Gerbier, T. Gherghetta, G. F. Giudice, M. Goodman, C. Grab, A. V. Gritsan, J. F. Grivaz, D. E. Groom, M. Grünewald, A. Gurtu, T. Gutsche, H. E. Haber, K. Hagiwara, C. Hagmann, K. G. Hayes, J. J. Hernández-Rey, K. Hikasa, I. Hinchliffe, A. Höcker, J. Huston, P. Igo-Kemenes, J. D. Jackson, K. F. Johnson, T. Junk, D. Karlen, B. Kayser, D. Kirkby, S. R. Klein, I. G. Knowles, C. Kolda, R. V. Kowalewski, P. Kreitz, B. Krusche, Yu V. Kuyanov, Y. Kwon, O. Lahav, P. Langacker, A. Liddle, Z. Ligeti, C. J. Lin, T. M. Liss, L. Littenberg, J. C. Liu, K. S. Lugovsky, S. B. Lugovsky, H. Mahlke, M. L. Mangano, T. Mannel, A. V. Manohar, W. J. Marciano, A. D. Martin, A. Masoni, D. Milstead, R. Miquel, K. Mönig, H. Murayama, K. Nakamura, M. Narain, P. Nason, S. Navas, P. Nevski, Y. Nir, K. A. Olive, L. Pape, C. Patrignani, J. A. Peacock, A. Piepke, G. Punzi, A. Quadt, S. Raby, G. Raffelt, B. N. Ratcliff, B. Renk, P. Richardson, S. Roesler, S. Rolli, A. Romaniouk, L. J. Rosenberg, J. L. Rosner, C. T. Sachrajda, Y. Sakai, S. Sarkar, F. Sauli, O. Schneider, D. Scott, W. G. Seligman, M. H. Shaevitz, T. Sjöstrand, J. G.

Smith, G. F. Smoot, S. Spanier, H. Spieler, A. Stahl, T. Stanev, S. L. Stone, T. Sumiyoshi, M. Tanabashi, J. Terning, M. Titov, N. P. Tkachenko, N. A. Törnqvist, D. Tovey, G. H. Trilling, T. G. Trippe, G. Valencia, K. van Bibber, M. G. Vincter, P. Vogel, D. R. Ward, T. Watari, B. R. Webber, G. Weiglein, J. D. Wells, M. Whalley, A. Wheeler, C. G. Wohl, L. Wolfenstein, J. Womersley, C. L. Woody, R. L. Workman, A. Yamamoto, W. M. Yao, O. V. Zenin, J. Zhang, R. Y. Zhu, P. A. Zyla, G. Harper, V. S. Lugovsky, P. Schaffner, Review of particle physics. *Phys. Lett. B* **667**, 1–6 (2008).

40. C. H. Park, D. J. Chadi, Effect of interstitial hydrogen impurities on ferroelectric polarization in $PbTiO_3$. *Phys. Rev. Lett.* **84**, 4717–4720 (2000).

41. H. Lee, T. H. Kim, J. J. Patzner, H. Lu, J.-W. Lee, H. Zhou, W. Chang, M. K. Mahanthappa, E. Y. Tsymbal, A. Gruverman, C.-B. Eom, Imprint control of $BaTiO_3$ thin films via chemically induced surface polarization pinning. *Nano Lett.* **16**, 2400–2406 (2016).

42. D. C. Sinclair, J. M. S. Skakle, F. D. Morrison, R. I. Smith, T. P. Beales, Structure and electrical properties of oxygen-deficient hexagonal $BaTiO_3$. *J. Mater. Chem.* **9**, 1327–1331 (1999).

43. R. D. Burbank, H. T. Evans, The crystal structure of hexagonal barium titanate. *Acta Crystallogr.* **1**, 330–336 (1948).

44. H. T. Langhammer, T. Müller, K. H. Felgner, H. P. Abicht, Crystal structure and related properties of manganese-doped barium titanate ceramics. *J. Am. Ceram. Soc.* **83**, 605–611 (2000).

45. N. X. Duong, J.-S. Bae, J. Jeon, S. Y. Lim, S. H. Oh, A. Ullah, M. Sheeraz, J. San Choi, J.-H. Ko, S. M. Yang, K.-H. Kim, I. W. Kim, C. W. Ahn, T. H. Kim, Polymorphic phase transition in $BaTiO_3$ by Ni doping. *Ceram. Int.* **45**, 16305–16310 (2019).

46. G. M. Keith, M. J. Rampling, K. Sarma, N. M. Alford, D. C. Sinclair, Synthesis and characterisation of doped 6H-$BaTiO_3$ ceramics. *J. Eur. Ceram. Soc.* **24**, 1721–1724 (2004).

47. R. E. Cohen, Origin of ferroelectricity in perovskite oxides. *Nature* **358**, 136–138 (1992).

48. R. Schaub, P. Thostrup, N. Lopez, E. Lægsgaard, I. Stensgaard, J. K. Nørskov, F. Besenbacher, Oxygen vacancies as active sites for water dissociation on rutile TiO_2 (110). *Phys. Rev. Lett.* **87**, 266104 (2001).

49. K. D. Kreuer, Aspects of the formation and mobility of protonic charge carriers and the stability of perovskite-type oxides. *Solid State Ion.* **125**, 285–302 (1999).

50. A. Hanada, K. Kinoshita, S. Kishida, Resistive switching by migration of hydrogen ions. *Appl. Phys. Lett.* **101**, 043507 (2012).

51. H. Han, C. Davis III, J. C. Nino, Variable range hopping conduction in $BaTiO_3$ ceramics exhibiting colossal permittivity. *J. Phys. Chem. C* **118**, 9137–9142 (2014).

52. G. Panchal, D. K. Shukla, R. J. Choudhary, V. R. Reddy, D. M. Phase, The effect of oxygen stoichiometry at the interface of epitaxial $BaTiO_3/La_{0.7}Sr_{0.3}MnO_3$ bilayers on its electronic and magnetic properties. *J. Appl. Phys.* **122**, 085310 (2017).

53. S. Majumder, P. Basera, M. Tripathi, R. J. Choudhary, S. Bhattacharya, K. Bapna, D. M. Phase, Elucidating the origin of magnetic ordering in ferroelectric $BaTiO_{3-\delta}$ thin film via electronic structure modification. *J. Phys. Condens. Matter* **31**, 205001 (2019).

54. M. Sheeraz, M. U. Rashid, A. Ali, F. Akram, H. J. Lee, J. San Choi, J.-S. Bae, Y. S. Kim, Y.-H. Shin, C. W. Ahn, T. H. Kim, Stabilization of 6H-hexagonal $SrMnO_3$ polymorph by Al_2O_3 insertion. *J. Eur. Ceram. Soc.* **41**, 5155–5162 (2021).

55. R. Yimnirun, J. Tangsritrakul, S. Rujirawat, S. Limpijumnong, Identification of Mn site in $BaTiO_3$ by synchrotron X-ray absorption spectroscopy measurements. *Ferroelectrics* **381**, 130–143 (2009).

56. J. F. Scott, Ferroelectrics go bananas. *J. Phys. Condens. Matter* **20**, 021001 (2007).

57. K. Parida, S. Das, P. K. Mahapatra, R. N. P. Choudhary, Relaxor behavior and impedance spectroscopic studies of chemically synthesized $SrCu_3Ti_4O_{12}$ ceramic. *Mater. Res. Bull.* **111**, 7–16 (2019).

58. W. Q. Cao, L. F. Xu, M. M. Ismail, L. L. Huang, Colossal dielectric constant of $NaNbO_3$ doped $BaTiO_3$ ceramics. *Mater. Sci. Poland* **34**, 322–329 (2016).

59. N. M. Beekmans, L. Heyne, Correlation between impedance, microstructure and composition of calcia-stabilized zirconia. *Electrochim. Acta* **21**, 303–310 (1976).

60. H. Näfe, Ionic conductivity of ThO_2- and ZrO_2-based electrolytes between 300 and 2000 K. *Solid State Ion.* **13**, 255–263 (1984).

61. J. R. Macdonald, E. Barsoukov, *Impedance Spectroscopy: Theory, Experiment, and Applications* (Wiley, 2005).

62. D. C. Sinclair, A. R. West, Impedance and modulus spectroscopy of semiconducting $BaTiO_3$ showing positive temperature coefficient of resistance. *J. Appl. Phys.* **66**, 3850–3856 (1989).

63. J. S. Choi, C. W. Ahn, J.-S. Bae, T. H. Kim, Identifying a perovskite phase in rare-earth nickelates using X-ray photoelectron spectroscopy. *Curr. Appl. Phys.* **20**, 102–105 (2020).

64. C. Miot, E. Husson, C. Proust, R. Erre, J. P. Coutures, X-ray photoelectron spectroscopy characterization of barium titanate ceramics prepared by the citric route. Residual carbon study. *J. Mater. Res.* **12**, 2388–2392 (1997).

65. D. E. Newbury, N. Ritchie, Electron-excited x-ray microanalysis at low beam energy: Almost always an adventure! *Microsc. Microanal.* **22**, 735–753 (2016).

66. A. C. Caballero, M. Villegas, J. F. Fernandez, M. Viviani, M. T. Buscaglia, M. Leoni, Effect of humidity on the electrical response of porous $BaTiO_3$ ceramics. *J. Mater. Sci. Lett.* **18**, 1297–1299 (1999).

67. R. N. Goldberg, N. Kishore, R. M. Lennen, Thermodynamic quantities for the ionization reactions of buffers. *J. Phys. Chem. Ref. Data* **31**, 231–370 (2002).

68. E. Sun, W. Cao, Relaxor-based ferroelectric single crystals: Growth, domain engineering, characterization and applications. *Prog. Mater. Sci.* **65**, 124–210 (2014).

69. F. Li, S. Zhang, D. Damjanovic, L. Q. Chen, T. R. Shrout, Local structural heterogeneity and electromechanical responses of ferroelectrics: Learning from relaxor ferroelectrics. *Adv. Funct. Mater.* **28**, 1801504 (2018).

70. N. Qu, H. Du, X. Hao, A new strategy to realize high comprehensive energy storage properties in lead-free bulk ceramics. *J. Mater. Chem. C* **7**, 7993–8002 (2019).

71. R. M. Glaister, H. F. Kay, An investigation of the cubic-hexagonal transition in barium titanate. *Proc. Phys. Soc.* **76**, 763–771 (1960).

72. S. M. Gaytan, M. A. Cadena, H. Karim, D. Delfin, Y. Lin, D. Espalin, E. MacDonald, R. B. Wicker, Fabrication of barium titanate by binder jetting additive manufacturing technology. *Ceram. Int.* **41**, 6610–6619 (2015).

73. H. Kim, A. Renteria-Marquez, M. D. Islam, L. A. Chavez, C. A. Garcia Rosales, M. A. Ahsan, T. L. B. Tseng, N. D. Love, Y. Lin, Fabrication of bulk piezoelectric and dielectric $BaTiO_3$ ceramics using paste extrusion 3D printing technique. *J. Am. Ceram. Soc.* **102**, 3685–3694 (2019).

74. G. Panchal, R. J. Choudhary, S. Yadav, D. M. Phase, Probing the effect of ferroelectric to paraelectric phase transition on the Ti-3*d* and O-2*p* hybridization in $BaTiO_3$. *J. Appl. Phys.* **125**, 214102 (2019).

75. L. Ni, M. Fu, X. Ren, Y. Zhang, Enhanced dielectric relaxations in spark plasma sintered $CaCu_3Ti_4O_{12}$ ceramics. *J. Mater. Sci. Mater. Electron.* **28**, 10191–10198 (2017).

76. Y. Wu, X. Zhao, J. Zhang, W. Su, J. Liu, Huge low-frequency dielectric response of (Nb, In)-doped TiO_2 ceramics. *Appl. Phys. Lett.* **107**, 242904 (2015).

77. Y. Song, P. Liu, W. Wu, Q. Zhou, High-performance colossal permittivity for textured (Al + Nb) co-doped TiO_2 ceramics sintered in nitrogen atmosphere. *J. Eur. Ceram. Soc.* **41**, 4146–4152 (2021).

78. S. Kim, H. J. Avila-Paredes, S. Wang, C.-T. Chen, R. A. De Souza, M. Martin, Z. A. Munir, On the conduction pathway for protons in nanocrystalline yttria-stabilized zirconia. *Phys. Chem. Chem. Phys.* **11**, 3035–3038 (2009).